To link to this article: DOI: 10.1149/1.3610401
URL: http://dx.doi.org/10.1149/1.3610401

To cite this version:

Larignon, C. and Alexis, Joël and Andrieu, Eric and Blanc, Christine and Odemer, Grégory and Salabura, Jean-Claude *Corrosion Damages Induced by Cyclic Exposure of 2024 Aluminum Alloy in Chloride-Containing Environments.* (2011) Journal of The Electrochemical Society (JES), vol. 158 (n° 6). pp. C284-C295. ISSN 0013-4651

Corrosion Damages Induced by Cyclic Exposure of 2024 Aluminum Alloy in Chloride-Containing Environments

C. Larignon,[a] J. Alexis,[b] E. Andrieu,[a] C. Blanc,[a,*,z] G. Odemer,[a] and J.-C. Salabura[a]

[a]*Université de Toulouse, CIRIMAT, UPS/CNRS/INPT, BP 44362, 31030 Toulouse cedex 4, France*
[b]*Université de Toulouse, INP/ENIT/LGP, BP 1629, 65016 Tarbes, France*

This paper focuses on the influence of cyclic exposure to chloride solutions on corrosion damage morphology developed on AA2024. The influence of the temperature during the air exposure periods was studied. Cyclic corrosion tests led to enhanced global corrosion damage compared to continuous immersion tests with residual mechanical properties of corroded samples significantly lower for cyclic tests. The corrosion morphology depended on the exposure conditions. For cyclic tests with air exposure periods at room temperature (CR tests), the corrosion defects were significantly longer; for a cyclic test with air exposure periods at $-20\,^{\circ}$C (CF tests), the propagation of corrosion defects was not promoted; however, the density of corroded grain boundaries was markedly increased. For CR samples, the corrosion damage observed was mainly explained taking into account electrochemical processes occurring at the tip of the defect which could be considered as an occluded zone characterized by a chloride-enriched electrolyte and H^+ reduction as major cathodic reaction. For CF tests, the interaction between the stresses induced by the phase transformation of the medium *i.e* solidification and the hydrogen enrichment of the substrate could be a possible mechanism explaining the evolution of the global mechanical properties of the corroded samples.

[DOI: 10.1149/1.3610401]

High-strength aluminum alloys such as those of the 2xxx series, *e.g.* 2024-T3 alloy, are widely used in the aircraft industry for the skin and wings of the aircraft even though they are susceptible to different forms of localized corrosion in chloride media such as pitting corrosion, intergranular corrosion, exfoliation and stress corrosion cracking.[1–12] In recent years, many studies have dealt with the corrosion behavior of aluminum alloys in chloride-containing solutions; many of these works focused on the influence of intermetallic particles on pitting and the transition from pitting to intergranular corrosion.[13–32] Concerning intergranular corrosion propagation, it is generally accepted that, in the 2xxx series alloys, intergranular corrosion is due to the presence of copper-rich intergranular precipitates in contact with a copper-poor precipitate-free zone (PFZ) adjacent to the grain boundaries. Intergranular corrosion is generally associated with a preferential dissolution of the PFZ due to both galvanic coupling between the PFZ and the precipitates and between the PFZ and the matrix.[6,7,9] Several factors have been identified that influence both morphology and initiation and/or propagation kinetics of intergranular corrosion. The alloy metallurgical state is considered as a first-order parameter. The authors thus identified both grain size and aspect ratio as important factors in controlling localized corrosion and especially intergranular corrosion.[9,33–35] The nature and the concentration of the aggressive media also play a significant role.[9,36] Mechanical stress also has a strong influence on localized corrosion.[11,34,35] Finally, the exposure conditions to the aggressive media are one of the major factors affecting the localized corrosion process. Strong differences in the intergranular corrosion morphology occur depending on the conditions of exposure to the aggressive media, *e.g.*, alternate immersion tests, exfoliation tests or intergranular corrosion tests.[37] Nevertheless, the effects of cyclic exposure to the corrosive environment have not been studied in detail yet despite the fact that, in actual use, aircraft structures are cyclically exposed to corrosive environments: when the plane is on the tarmac, it is exposed to a corrosive environment and sometimes to high temperatures but, during a flight, exposure to the corrosive environment decreases and, for some parts of the structure, the temperature falls to roughly $-50\,^{\circ}$C, while others are maintained at room temperature or more. Thus, real conditions correspond to cyclic exposure to an aggressive medium with or without exposure to very cold temperatures.

The present work aims to reproduce real exposure conditions as closely as possible. It was focused on the characterization of the corrosion damages induced on AA2024 during cyclic exposures to chloride-containing solutions. Two kinds of cyclic corrosion tests were performed, *i.e.*, cyclic corrosion tests at room temperature and cyclic corrosion tests with exposure to low temperatures. It was assumed that the exposure to very cold temperatures of aluminum structures during an aircraft service life could influence the corrosion behavior of the material mainly due to the solidification of the electrolyte trapped in the corrosion defects. The influence of the cooling rate was not considered. The results were compared to those obtained with continuous immersion tests. The corrosion damage was first characterized by measuring the residual mechanical properties of the pre-corroded samples to have a global evaluation of the damage. Further description of the corrosion damage induced by cyclic exposure to chloride solutions was obtained by using optical and scanning electron microscope observations; the morphology of the intergranular damage was statistically described based on local observations of more than 100 corrosion defects for each exposure conditions. The present work also attempted to bring relevant results to explain differences in the corrosion damages induced by cyclic exposure to chloride solutions compared to continuous immersion conditions. An experimental device was specifically developed to help us in understanding the results; the experimental set-up allowed to measure the deflection of a single side corroded plate as a function of the temperature by using a laser beam extensometer. It assessed the mechanical stresses induced by the solidification of the electrolyte trapped in the corrosion damage during exposure to freezing temperatures and enabled the chloride concentration of the electrolyte to be determined for each exposure condition. Open circuit potential and electrochemical impedance spectroscopy measurements were also performed to supplement the results obtained with this original device.

Experimental

Material.— Corrosion investigations were performed on 2024 T351 aluminum alloy supplied in the form of a 50 mm thick rolled plate. Its composition is given in Table I. The T351 temper consists of a solid-solution heat treatment at $495\,^{\circ}$C ($\pm 5\,^{\circ}$C), water quenching, straining and tempering at room temperature for four days. The microstructure of the material presented grains elongated along the rolling direction (L) (Fig. 1a). Average grain sizes in the longitudinal, long transverse (LT) and short transverse (ST) directions were 700, 300 and 100 μm respectively. Analysis and observations of the microstructure with a scanning electron microscope (SEM) and a transmission electron microscope (TEM) showed both intragranular precipitates such as Al-Cu-Mn-Fe and Al_2CuMg particles and intergranular precipitates (mainly Al_2CuMg and Al-Cu-Mn precipitates)

---

[*] Electrochemical Society Active Member.
[z] E-mail: christine.blanc@ensiacet.fr

Table I. Chemical composition of 2024 T351 aluminum alloy (wt %).

Alloying element	Al	Cu	Mg	Mn	Fe	Si	Ti
% weight	Base	4.464	1.436	0.602	0.129	0.057	0.030

(Fig. 1b) in good agreement with the literature.[6] No precipitate-free zone (PFZ) was observed along the grain boundaries on the as-received plate; however, it was revealed after heat treatment. These observations were consistent with the results of Zhang and Frankel who showed that a PFZ was visible for a T8 temper but not for a T3 temper.[4]

Corrosion tests.—Cyclic corrosion tests were performed to reproduce as closely as possible the environment exposure conditions of the 2024-T351 aluminum alloy of the aircraft skin. The electrolyte for all corrosion tests consisted in a 1 M NaCl solution prepared with Rectapur chemicals dissolved in deionized water. This electrolyte was chosen since chloride ions are among the most aggressive species present in the aircraft environment. Tests were carried out on both tensile specimens to globally evaluate the corrosion damages by measuring the degradation of mechanical properties and on cubic samples to observe and characterize at a local scale the corrosion defects size and distribution (Fig. 2). All samples were extracted from the core of the plate. For tensile specimens, the ST-LT plane was exposed to the electrolyte; the mechanically bearing section was the LT-L plane with corrosion defects propagating in the L direction which was the most critical direction for corrosion propagation. For cubic samples (10 mm edge), the ST-LT plane was exposed to the electrolyte in order to observe and quantify the corrosion induced damage propagating in the L direction. Before corrosion tests, the samples were mechanically polished with different grade SiC papers up to 4000 grade, then rinsed in distilled water and air-dried. All corrosion tests were conducted in a laboratory room with controlled temperature (T = 22 °C). The hygrometry was measured during the testing period (51% relative humidity). Moreover, to avoid temperature fluctuations of the electrolyte due to the size of the laboratory room, the temperature of the electrolyte was also controlled and maintained at 22 °C by using a thermostat-cryostat. Four exposure conditions were studied with two cyclic corrosion tests and two continuous immersion tests. During the immersion periods, the samples were hung in the corrosion cell by using a thin nylon yarn. A cyclic corrosion test consisted of three cycles of 24 h; each cycle was composed of an 8-h immersion in the electrolyte followed by a 16 h air exposure period at the temperature of the laboratory room *i.e.*, 22 °C for the Cyclic Room (CR) test and at −20 °C for the Cyclic Freezing (CF) test. During the air exposure periods, the samples were hung by using the nylon yarn in a container placed in the laboratory room for the CR tests and, for the CF tests, the samples were hung in a container maintained at −20 °C. The two continuous immersion tests were considered as controls. The first lasted 24 h, which corresponded to the cumulated time of immersion for the cyclic corrosion tests, and the second lasted 72 h, which corresponded to the duration of the whole cyclic corrosion test. For CR tests, additional experiments using a microbalance were carried out to evaluate the time the electrolyte trapped inside the corrosion defects needed to evaporate during the air exposure periods. Samples were first exposed to 2 cycles immersion/air exposure period at room temperature and then immersed again in 1 M NaCl for 8 h. Immediately after the last immersion period, they were put on a balance placed in the container and their weight was measured as a function of time. The corroded sample weight rapidly decreased for the first 8 h and then became stable, which might show that 8 h after the beginning of the air exposure period, a large part of aqueous electrolyte trapped inside the corrosion defects was evaporated. Thus, it was assumed that, even if corrosion defects could remain wet during the air exposure periods, the electrolyte evaporation was sufficient enough to partially dry the corrosion products and generate a concentration increase of the chemical species trapped inside the corrosion defects. Concerning the CF tests, preliminary measurements showed that the melting temperature of a chloride solution varied between 2 and −16 °C for chloride concentrations ranging from 0 to 5 M (Fig. 3). The melting temperature was determined during the warming up of frozen solutions and an over-melting phenomenon explained the positive temperature measured for deionized water. Thermal loss certainly also contributed to explaining the results. Since a 5 M concentration corresponded to the maximum solubility of sodium chloride in water at room temperature, it was assumed that the electrolyte trapped in the corrosion defects was frozen during the air exposure periods at −20 °C whatever its chloride concentration. Moreover, taking into account d the thermal diffusivity of aluminum alloys which is in the range of $8 \cdot 10^{-5}$ $m^2.s^{-1}$ and x the depth affected by the electrolyte penetration which was fixed to 500 μm (higher than the observed value, see the experimental part), the cooling time t can be roughly estimated as $t = x^2/d \approx$ 3 ms. Consequently, due to the small size of the samples, the electrolyte trapped in the intergranular corrosion defects was frozen immediately at the beginning of the air exposure period at −20 °C. Since no electrochemical processes could occur at −20 °C, the associated effective corrosion duration was assumed to last 24 h. After the corrosion tests, both cubic samples and tensile specimens were thoroughly rinsed with distilled water, cleaned using an ultrasonic bath and air-dried.

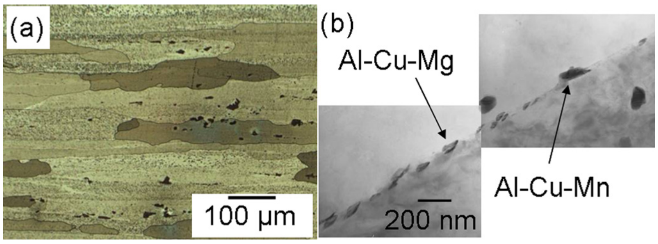

Figure 1. (Color online) Microstructure of AA 2024 (a) optical microscope observation (b) transmission electron microscope observation of a grain boundary.

Evaluation of the residual mechanical properties of the corroded samples.—Tensile tests were performed on tensile specimens with an Instron testing machine equipped with a 5 kN load cell and a constant strain rate of 10^{-3} s^{-1}. Tests were performed for both non-corroded and corroded samples. For each exposure condition, three tensile specimens were tested to check the reproducibility of the results.

Characterization of intergranular corrosion damage morphology.—After the corrosion tests, each cubic sample was cut along the ST-L plane to obtain four slices; each slice was polished down to 1 μm diamond paste and then observed using an optical microscope. All the intergranular defects propagating in the L direction, *i.e.* perpendicularly to the ST direction, were counted and their penetration depth measured. Taking into account the cumulative length of corroded surface observed in the ST direction, *i.e.* 40 mm, and the grain size in this direction, estimated at 100 μm, almost 400 grain boundaries were analyzed in one cubic sample. For cyclic corrosion tests, due to the high number of corrosion defects (see results), only one cubic sample was analyzed for each cyclic test. However, since the number of corroded grain boundaries was lower for continuous immersion tests than for cyclic corrosion tests (see results), two cubes (*i.e.*, 80 mm = 800 grain boundaries) were analyzed for continuous immersion tests. Four parameters were considered as relevant to describe the intergranular corrosion morphology and were statistically determined: the ratio of corroded grain boundaries, the average and maximal depth of intergranular defects and the cumulative length of corroded grain boundaries (taking into

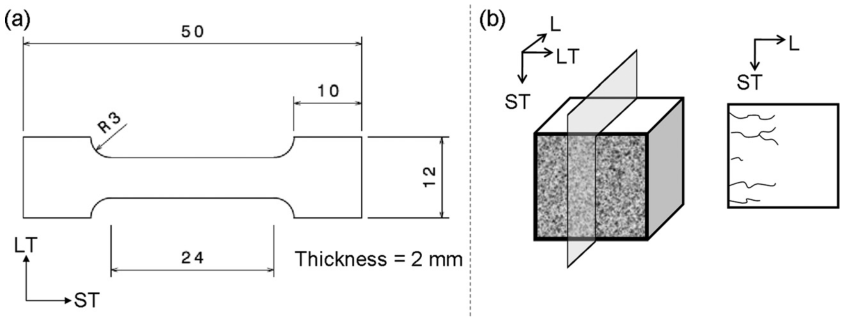

Figure 2. Schema of (a) tensile specimens and (b) cubic samples (size in mm).

account the cumulated length analyzed *i.e.* 40 or 80 mm). The ratio of corroded grain boundaries corresponded to the ratio of corroded grain boundaries emerging in the ST-LT plane to the total number of grain boundaries observed. The depth of penetration of an intergranular defect was measured as the distance between the sample surface and the deepest point along the corrosion defect path. The cumulative length of corroded grain boundaries was obtained by adding the length of each intergranular defect observed on the sample. Moreover, observations with a Field Emission Gun Scanning Electron Microscope (FEG SEM-7000 F from JEOL with the incident electron beam kept between 10 and 15 kV) were also carried out to carefully examine the corrosion defects. For some, elemental spot analyses were performed with a SDD Bruker X'flash energy dispersive X-Ray spectrometer (EDX).

Electrochemical measurements.—Open circuit potential (OCP) and electrochemical impedance spectroscopy (EIS) measurements were performed using a Biologic potentiostat/galvanostat equipped with EC-Lab software and an impedance module. For all acquisitions, the working cell had a conventional three electrode construction with a platinum counter electrode and a saturated calomel electrode as reference and the AA2024 sample as working electrode. The potential range was fixed to $[-1; +1]$ V in order to obtained a resolution of 50 μV. The experiments were composed of two sequences, the first one to measure the OCP (Open Circuit Potential) value and the second one to plot impedance diagrams of the sample studied in 1 M NaCl solution at 22 °C. Thus, first the OCP values were plotted every second during twenty minutes to obtain a stabilized value. The potential was then fixed to this latest value during ten minutes before starting impedance measurements. Impedance measurements were performed using as disturbance a sinusoidal potential of an amplitude limited to 7 mV (5 mV rms). The acquisition parameters were adapted depending on the frequency range to improve the accuracy of the results. The frequency range varied between 3 kHz and 1 Hz with 10 points per decade. For continuous immersion tests, OCP and EIS measurements were performed as a function of the immersion time (24, 48 and 72 h). For Cyclic tests, OCP and EIS plots were carried out at the beginning and at the end of each immersion period.

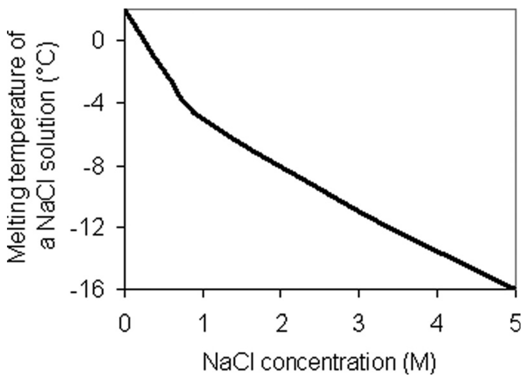

Figure 3. Melting temperature of NaCl solutions versus chloride content.

Hydrogen content measurements.—Average hydrogen concentration was measured by using an Instrumental Gas Analysis (IGA) on a Horiba EMGA-621 W analyser. This technique measured the total amount of hydrogen contained in a solid aluminum sample by melting it at 950 °C. The hydrogen content (expressed in ppm by weight) was then estimated using the thermal conductivity method. Pure argon was used as a carrier gas.

Development of New Experimental Device

An experimental device (deflection test) was specifically developed in this work to determine whether the solidification of the electrolyte trapped inside the intergranular corrosion defects during sample exposure to low temperatures equal to −20 °C (*i.e.* during air exposure periods for CF tests) could lead to significant mechanical stresses applied on the walls and tip of the corrosion defects. Figures 4a and 4b show schematics of the experiment and the experimental device. The experimental procedure was the following: a 1 mm thick parallelepipedic sample (50×10) (mm) was cut in the L direction of the 2024 aluminum plate and submitted to a CF test (step 2 in Fig. 4a) with one side of the sample previously protected by a varnish in order to develop corrosion defects only on the other side (step 1 in Fig. 4a). After corrosion test (step 2, propagation of the corrosion defects along the L direction), the corroded specimen was superficially dried and placed in a Dewar flask filled with liquid nitrogen to freeze the remaining electrolyte trapped inside intergranular corrosion defects (step 3 in Fig. 4a). A thermocouple probe was connected to the specimen to record its temperature (Fig. 4b). Due to the solidification of the electrolyte trapped inside the corrosion defects, volume expansion occurred generating mechanical stresses inside the intergranular corrosion defects. When the mechanical stresses were significant, they made the plate bend since only one of the sample faces was corroded. The deflection of the corroded sample was then measured using a laser beam. An alumina pin was attached at the top of the corroded specimen to magnify the deflection and, at the top of the alumina pin, a perfectly polished alumina target was fixed. The laser beam was shone on the target to measure the deflection of the corroded specimen. The zero position corresponded to the deflection at low temperature. If mechanical stresses due to the solidification of the electrolyte were applied inside the corrosion defects, the sample was thus bent at the beginning of the experiment. The position of the target, *i.e.* the deflection of the corroded specimen, was then recorded as the temperature rose. When the melting point of the electrolyte trapped inside the intergranular defects was reached, the corroded specimen was no longer submitted to mechanical stresses and the deflection (if it occurred) of the corroded specimen became equal to zero so that a sharp variation of the target position was measured. If no mechanical stress was applied due to the volume expansion of the electrolyte, the position of the target should remain nearly stable. Four

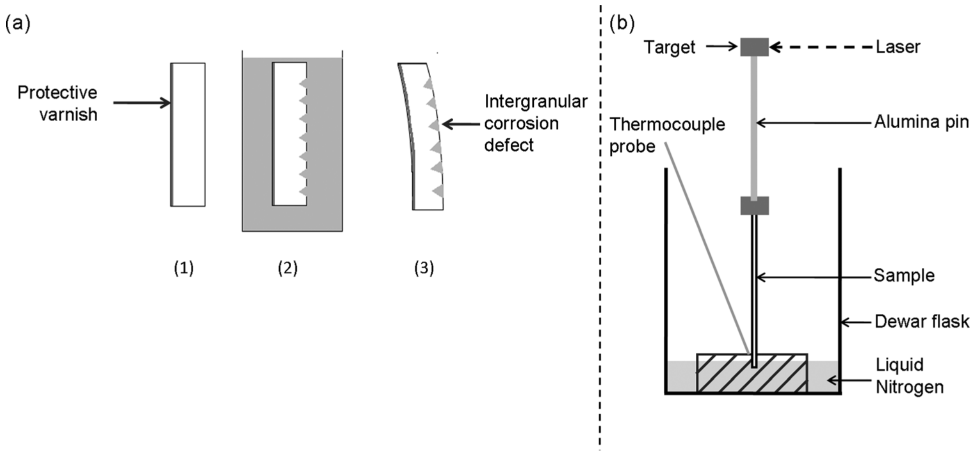

Figure 4. (a) Principle schema of the deflection test: (1) protection towards corrosion of the sample on one face (2) corrosion tests of the sample followed by the growth of intergranular corrosion defects on the non-protected face (3) exposure of the sample to very cold temperatures, solidification of the electrolyte trapped inside the corrosion defects followed by sample deflection (b) Schema of the experimental device.

experiments were performed for samples submitted to a CF test and the results were compared to those obtained with a non-corroded specimen. For more clarity, only two sets of curves are given.

Measurements of the chloride concentration inside the corrosion defects.—This experimental device (Fig. 4) was also used to measure the chloride content of the electrolyte trapped inside the corrosion defects for each exposure conditions (24 and 72 h continuous immersion tests, CR and CF tests). The temperature for which a sharp variation of the target position was detected was identified as the melting temperature of the electrolyte trapped inside the corrosion defects. Figure 3 allowed then to relate the measured temperature to the chloride concentration of the solution. For each exposure conditions, experiments were carried out four times. For more clarity, only two sets of representative curves are given.

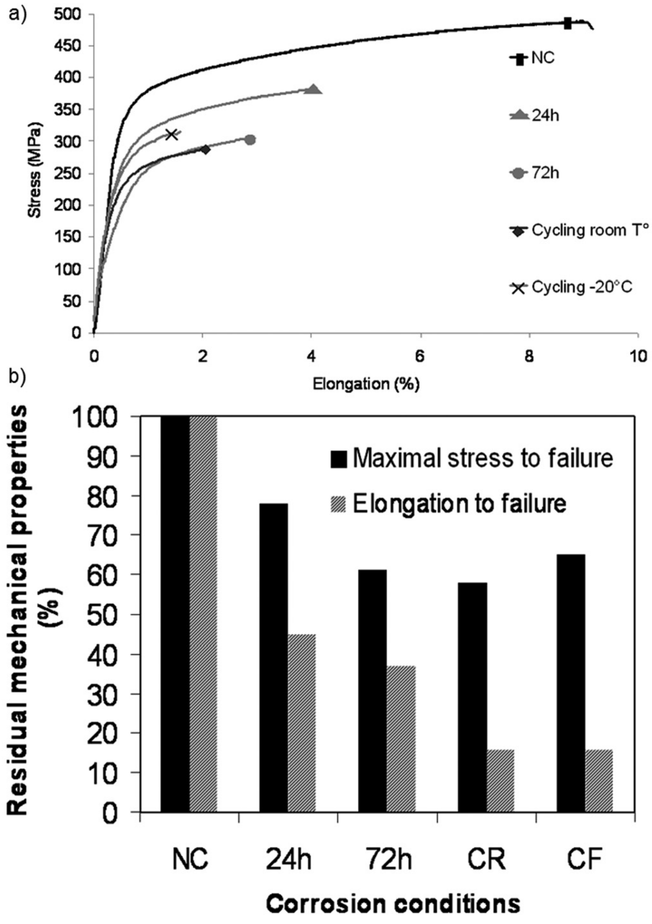

Figure 5. (a) Representative tensile curves and (b) residual mechanical properties of AA2024 after continuous immersion tests (24 and 72 h) and cyclic (CR and CF) corrosion tests. NC corresponds to tensile tests performed on non-corroded samples.

Experimental Results and Discussion

Residual mechanical properties of the corroded samples.—The corrosion damage due to the exposure to chloride solutions was first characterized by measuring the residual mechanical properties of the corroded samples. This led to a global evaluation of the damage, which was representative since the volume of material tested contained a very large number of grain boundaries. Figure 5 shows the results of the tensile tests performed on pre-corroded specimens. Tests were also performed on non-corroded specimens and the results obtained are reported for comparison. Figure 5a shows representative tensile curves obtained for each exposure condition. Except for a 72 h continuous immersion test, the shape of the tensile curve was exactly the same: in the elastic domain, the curves were superimposed and they had the same shape in the plastic domain with a shift towards a lower maximal stress to failure when the sample was corroded by comparison to a non-corroded specimen. This showed, at first, that the corroded samples and the non-corroded ones had the same mechanical behavior law in tension. Moreover, this also showed that the propagation of intergranular corrosion could be considered as the growth of a mechanically non-bearing zone.[8] Therefore, the maximal stress to failure of the material was chosen as a relevant parameter to evaluate the corrosion damages after exposure to chloride solutions. Comparison to a non-corroded specimen provides the depth of the corroded zone as shown by Augustin et al.[8] Figure 5b gives mean residual mechanical properties measured from three samples (*i.e.*, three tensile curves) for each exposure condition. The normalized residual mechanical properties were defined as the ratio (in percentage) of the values measured for a corroded specimen to that for a non-corroded sample. It was found that exposure to chloride solutions led to a decrease of the normalized residual mechanical properties whatever the corrosion testing conditions were. Elongation to failure corroborated the results since this mechanical property was also significantly reduced after all corrosion tests by comparison to a non-corroded sample. This showed that the elongation to failure is another relevant parameter to globally evaluate the corrosion damage. Comparison of the residual maximal stress to failure obtained for 24-h and 72-h continuous immersion tests showed that an increase of the immersion time led to a decrease of the maximal stress to failure, which showed an extended corrosion damage for longer immersion time. Comparison of the values of the elongation to failure obtained for both continuous immersion tests corroborated the results. It was also shown that the mean maximal stress to failure measured after CR tests was lower than the values obtained after a 24 and/or 72-h continuous immersion tests; the elongation to failure for a CR specimen was dramatically lower by comparison to the values measured after 24 h and/or 72 h continuous immersion tests. For CF test, the residual maximal stress to failure was lower than that for a 24 h-immersion test but slightly higher than for a 72 h-immersion test. However, as said previously, for CF test, dissolution processes only occurred for 24 h; moreover, as for CR tests, the elongation to failure was dramatically low for CF samples. Therefore, the results of tensile tests showed that cyclic corrosion tests were more damaging for AA2024 than continuous immersion tests. Moreover, CR and CF tests seemed to lead to a similar damage from a global mechanical point of view.

Morphology of intergranular corrosion defects versus corrosion testing conditions.—Observations using optical and scanning electron microscopes were also performed to obtain a local description of the damage with characterization of the corrosion defects morphology. Figure 6 shows FEG SEM observations of intergranular defects observed on AA 2024 after a 24 h continuous immersion test (Fig. 6a), a 72 h continuous immersion test (Fig. 6b), a CR test (Figs. 6c and 6d) and a CF test (Figs. 6e and 6f). Comparison of Figs. 6a and 6b shows that an increase of the immersion time led to a significant increase of the width of the corrosion defects. Comparison of Figs. 6a and 6b for one part and Figs. 6c, 6d, 6e and 6f for another part showed that the intergranular defects that developed during a cyclic corrosion test were more branched out than those formed during continuous immersion tests. Moreover, while only the grain boundaries were corroded during continuous immersion tests, it was observed that, after cyclic tests, when grain boundaries were corroded, the adjacent subgrain boundaries were found to be corroded too (Figs. 6d and 6f). As explained in the experimental section, cubic samples were also observed by using optical microscopy and the morphology data were statistically analyzed. Table II sums up the results obtained for the four exposure conditions. Comparison of the results obtained for the 24-h and 72-h immersion tests showed that an increase of the immersion time led to a slight increase of the ratio of corroded grain boundaries and of the average depth of the corrosion defects. The maximal depth of the intergranular defects and the cumulative length of corroded grain boundaries were also higher after a 72 h immersion test compared to a 24 h test. The evolution of all these statistical parameters with increasing immersion time corroborated the degradation of the mechanical properties, in particular for the stress to failure. Moreover, previous observations showed that an increase of the immersion time led also to an increase of the width of the corrosion defects which also contributed to explain the mechanical data. Indeed, the decrease of the stress to failure was associated to the growth of a mechanically non-bearing zone; this was attributed to the growth of depth and width of the corrosion defects. For further details, the distribution of the intergranular corrosion defect size was plotted to help in understanding the statistical data (Fig. 7). No significant difference was observed between the 24 and 72 h distributions (Figs. 7a and 7b) except for some long defects observed after a 72-h immersion test. These rare long corrosion defects as well as the increase of the width of the corrosion defects when the immersion time increased might explain the singular shape of the tensile curves observed after a 72-h immersion test and particularly the slope of the curve in the elastic domain (Fig. 5a). It could be assumed that, after a 72-h immersion, the corrosion defects were opened enough to artificially modify the apparent material stiffness. Concerning the CR samples, Fig. 7c showed that the ratio of corroded grain boundaries, the average depth, the maximal depth and the cumulative length of intergranular defects were higher than the continuous immersion tests. Figure 7c also showed that the proportion of long defects was higher for CR tests compared to continuous immersion tests, which might reveal that CR exposure enhances the propagation of some intergranular defects. The morphology data were therefore in agreement with the tensile tests results (Fig. 5); CR test was found to significantly enhance the corrosion damage of AA2024. For CF immersion tests, the ratio of corroded grain boundaries was higher than those measured for the other tests, even for the CR tests, while the average and maximal depths of the corrosion defects were lower than those measured for the other tests even for a 24-h immersion test. The CF test seemed to promote the initiation of intergranular defects while their propagation was not favored by comparison with continuous immersion tests and/or CR tests. This was confirmed by the distribution of the intergranular corrosion defect sizes which revealed a large number of short defects with one third of the defects shorter than 20 μm (Fig. 7). The cumulative length of the corrosion defects was significantly higher for CF tests compared to continuous immersion tests due to enhanced initiation of numerous intergranular defects. Therefore, the morphology data of the corrosion defects for CF test could not totally explain the significant degradation of the mechanical properties observed (Fig. 5) despite of the high number of corroded grain boundaries. The low values of the mean and maximal depth of the corrosion defects were quite in good agreement with the stress to failure measured. However, it was difficult to explain, from the statistical data, the low value of the elongation to failure measured after CF test. This ostensible opposite trend between the characterization of the intergranular defect morphology and the residual mechanical properties of the CF samples suggested that a volumic degradation of the material could occur at the tip of the defect. Pantelakis et al. proposed that a hydrogen-affected zone existed at the tip of the intergranular defect, which could explain the significant decrease of the mechanical properties of AA2024 after CF tests.[37] Therefore, hydrogen embrittlement could be a possible mechanism to explain the singular behavior of CF samples compared to samples exposed to continuous immersion tests or to CR tests. This degradation mechanism would imply a large production of hydrogen at the tip of the corrosion defect and, above all,

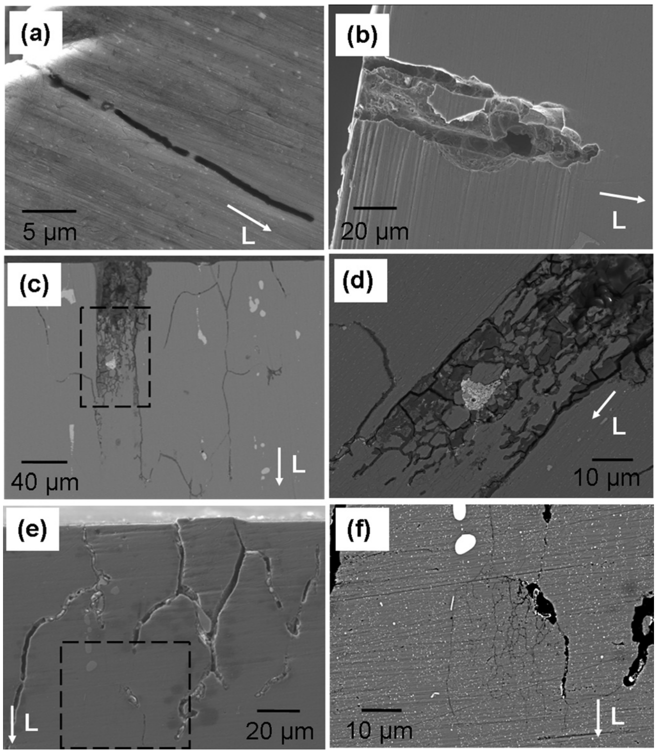

Figure 6. FEG SEM observations of corroded AA2024 samples. Representative morphology of intergranular corrosion defects developed during (a) 24-h continuous immersion test, (b) 72-h continuous immersion test (c) CR test (d) CR test (close-up), (e) CF test and (f) CF test (close-up).

Table II. Statistical analysis of the data concerning the intergranular corrosion morphology for continuous and cyclic corrosion tests.

Corrosion test	24 h	72 h	CR	CF
Number of corroded grain boundaries/number of grain boundaries observed	0.16	0.19	0.35	0.46
Arithmetic mean depth (μm)	69	72	111	53
Maximal depth (μm)	313	380	430	246
Total analyzed length (mm)	82.8	82.8	41.5	49.2
Number of defects observed	133	138	106	193
Cumulative corroded length/Total analyzed length (mm/mm)	0.09	0.15	0.57	0.35

hydrogen diffusion into the material. Table III shows the hydrogen content measurements performed for the corroded samples compared to non-corroded ones. The hydrogen content was higher for a CF specimen while the statistical data globally showed a lower extent of the corrosion damage with, for example, a cumulative corroded length lower than for a CR specimen. The amount of corrosion products was thus found to be insufficient to explain such a high amount of hydrogen in CF samples; it was then necessary to assume that hydrogen had been produced and penetrated into the material. It is worth mentioning that, if mechanical stresses were present inside the corrosion defects, hydrogen diffusion could be enhanced. Therefore, in order to understand the differences observed from both a mechanical point of view and corrosion defect morphology results between the different exposure conditions, further observations of the corrosion defects were performed and a new experimental device was developed to study the mechanical stresses and measure the chloride concentration inside the corrosion defects. The results obtained were compared to those obtained by OCP and electrochemical impedance spectroscopy measurements.

SEM and TEM observations of the corrosion defects.— Even though different corrosion morphologies were found for the different corrosion conditions, a common feature was observed whatever the corrosion test *i.e*., for all samples, corroded coarse intermetallic particles were observed along the corroded grain boundaries. Figure 8 shows a FEG-SEM observation of a corroded specimen with grain boundaries lined with voids. Void volume may have been occupied by intermetallic particles as suggested by the intermetallic remnants observed in a few voids. The result was fully consistent with the literature concerning co-operative corrosion *i.e.* intermetallic particle reactivity and intergranular corrosion.[27–31,38] EDS analyses performed on sites 1, 2 and 3 in Fig. 8c indicated copper enrichment of the particles composed of more than 80 atom % of copper while, for the surrounding corrosion products, the copper content decreased to 17 atom %. This evolution can be related to that of oxygen composition which was about 1, 4 and 44 atom % for sites 1, 2 and 3 respectively. Electrochemical activity localized on intermetallic particles on the material surface has often been reported in the literature: the corrosion behavior of intermetallic particles changes from anodic to cathodic with Al and Mg dealloying leading to the formation of copper-rich remnants on which enhanced oxygen reduction occurs. This leads to a local pH increase which explains the dissolution of the surrounding matrix.[13–32,39–41] Electrochemical activity thus initiated on the intermetallic particles present at the material surface and was then driven into the grain boundaries.[27–31,38] Intergranular corrosion propagation could then been partly associated with coarse intermetallic particle activity present in the grain boundaries.[42] This suggested inward diffusion of chloride ions and/or oxygen from the surface and along the grain boundaries. The strong dissolution observed for the subsurface coarse intermetallic particles suggested a different mechanism than that described above. As suggested by King et al., the selective dissolution of subsurface intermetallic particles was assumed to release Al^{3+} cations which undergo hydrolysis and lead to local acidification.[38] However, electrochemical activity localized on subsurface coarse intermetallic particles is not sufficient to explain intergranular corrosion propagation due to the distance from one particle to another in the grain boundaries. The reactivity of the small intergranular S-phase particles which decorated the grain boundaries (Fig. 1b) and galvanic coupling between these particles and the surrounding matrix cannot be ignored.[6,7,9,43] TEM observation of a corroded grain boundary after 72 h immersion in 1 M NaCl clearly showed the complete dissolution of the small intergranular S-phase particles which suggests highly aggressive chemical conditions in the corrosion defects and the same acidic mechanism as that previously proposed (Fig. 9a). Moreover, TEM observations showed the presence of an oxide film on the wall of the corrosion defects while a fresh metal surface was observed at the tip of the defect (Fig. 9b). It was thus assumed that there was a gradient concerning the aggressiveness of the electrolyte trapped in the corrosion defect and particularly a pH gradient with very acidic pH deep inside the defect leading to the dissolution of the aluminum solid solution and impeding its possible repassivation.[30] Furthermore, a close-up of the oxide film grown on the corrosion defect walls showed the presence of a copper-rich film at the metal/oxide interface (Fig. 9c) confirmed by EDS analysis (Fig. 9d) and in accordance with previous works performed on anodic films formed on Al-Cu alloys.[44–47] Local galvanic coupling between the corrosion defect wall and the depth of the defect could then be considered with high cathodic activity on the copper-enriched defect walls while the tip of the defect acted as an anodic site. Therefore, a mechanism involving the transition from an alkaline to an acidic dissolution process for S-phase particles (coarse and small intergranular particles) could be assumed. Intergranular corrosion was initiated due to surface coarse intermetallic particle activity combined with enhanced oxygen reduction on copper-rich remnants. It probably propagated due to the reactivity of subsurface coarse intermetallic particles and small intergranular particles leading to the establishment of a very acidic intergranular corrosion front correlated to another intermetallic particle dissolution mechanisms involving Al^{3+} cation hydrolysis. At the intergranular corrosion front, the highly acidic pH destabilized the aluminum solid solution leading to its dissolution and probably additional H^+ production correlated to the hydrolysis of Al^{3+} from the matrix. So, while the anodic reaction corresponded to the aluminum oxidation, the cathodic reactions were probably oxygen reduction on the alloy surface and, when the intergranular corrosion propagated, due to the local acidification at the tip of the corrosion defect, H^+ reduction inside the corrosion defect leading to the production of hydrogen.[30] However, oxygen reduction on the walls of the corrosion defects could be a possibility but its occurrence was higher when the depth of the intergranular corrosion defects was lower and their width higher as suggested by Knight et al.[48] Hydrogen content measurements (Table III) revealed higher hydrogen content in corroded samples by comparison with the results obtained in non-corroded samples; this could corroborate the assumption concerning the high acidification at the intergranular corrosion front followed by hydrogen penetration into the material. However, it was necessary to take into account that a part of the hydrogen detected was contained in the corrosion products. But, as explained previously, results obtained for CF tests showed that the hydrogen contained in the corrosion products could not explain the high amount of hydrogen measured showing that extensive H^+ production had really occurred. Subsequent H^+ reduction led to hydrogen generation which penetrated inside the metal for CF samples. For the other

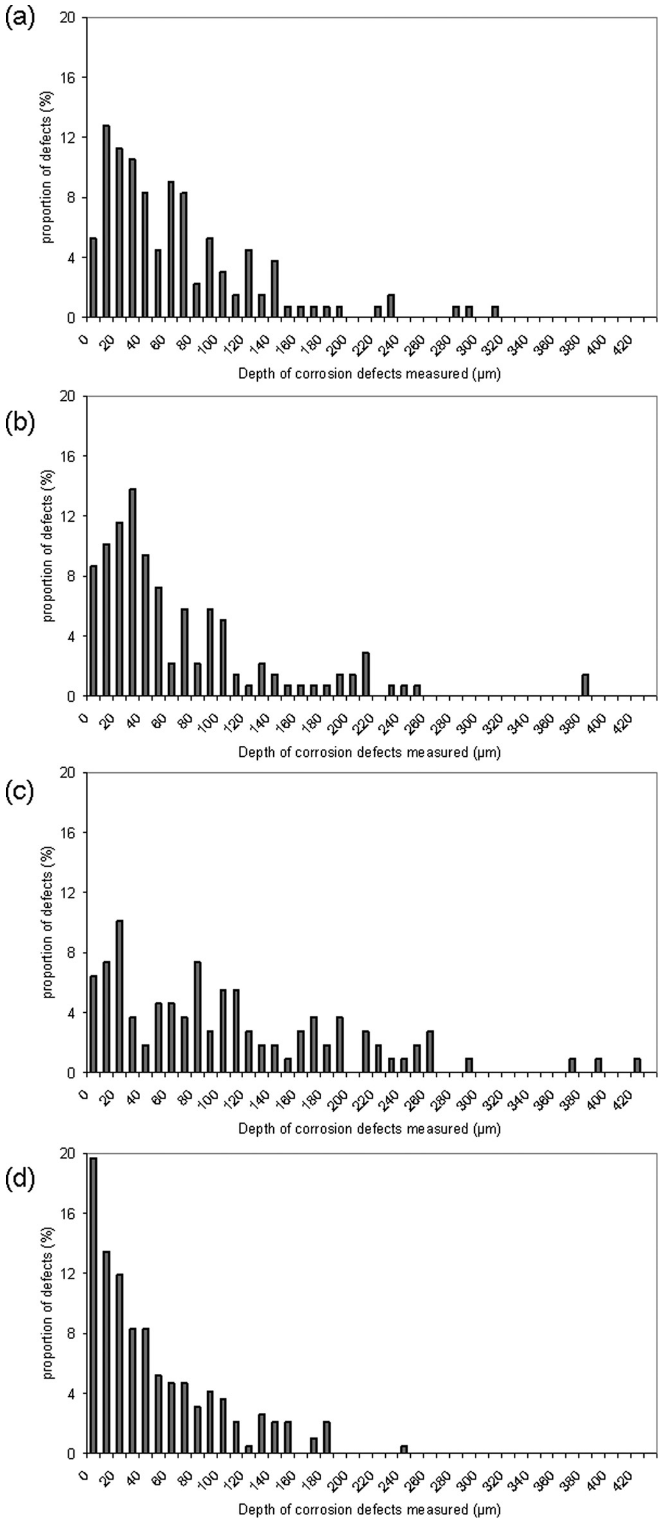

Figure 7. Distribution of the intergranular corrosion defect size for (a) a 24-h continuous immersion test (b) a 72-h continuous immersion test (c) a CR test and (d) a CF test.

corrosion conditions, the amount of hydrogen in the material was lower but, statistical data concerning the morphology of the corrosion defects showed that the dissolution processes were stronger. It was thus assumed that the high acidification at the tip of the corrosion defects was a common feature for all corrosion tests even if the hydrogen generated by H^+ reduction penetrated more (maybe penetrated only) into the alloy for CF specimens. Furthermore, a chloride concentration gradient could also be expected, for all corrosion tests, due to electroneutrality reasons and resultant chloride ion migration towards the intergranular corrosion front generating a high chloride concentration in the depth of the defect.

Table III. Hydrogen content measurements for non corroded and corroded samples.

Corrosion test	Non corroded	24 h	72 h	CR	CF
Hydrogen content (ppm)	4–12	11	23	24–25	48–89

Evaluation of the mechanical stresses inside the corrosion defects.—In the literature, some authors assumed that the corrosion products trapped inside the corrosion defects could generate mechanical stresses leading to enhanced corrosion damage.[49–52] Mechanisms proposed in the literature for exfoliation, which is promoted in humid or cyclic exposure conditions, showed that crack opening stresses are possible during cyclic tests because of partial drying of the corrosion products. Moreover, results from the literature showed that exfoliation corrosion also occurred during full immersion in EXCO solutions, which indicated that even the wet corrosion products can generate enough opening stress to accelerated intergranular attack. However, results obtained in this work (mechanical data

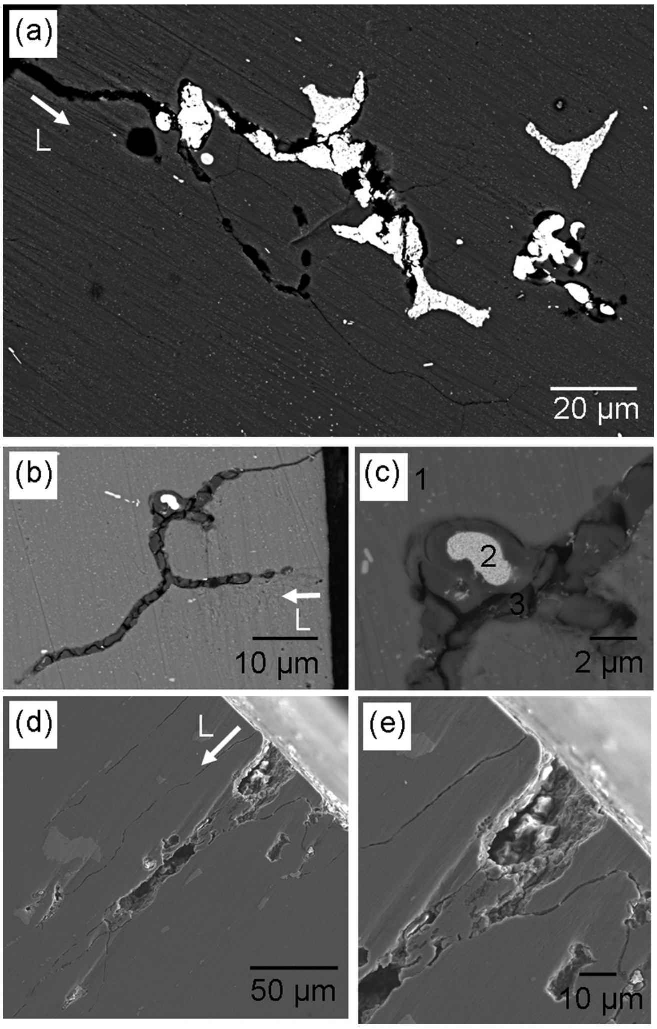

Figure 8. FEG-SEM observations of an AA 2024 sample after (a) 24-h continuous immersion in 1 M NaCl (b) CF test, global view (c) CF test, close-up on the dealloying precipitates (d) CR test, global view (e) CR test, close-up on the damage.

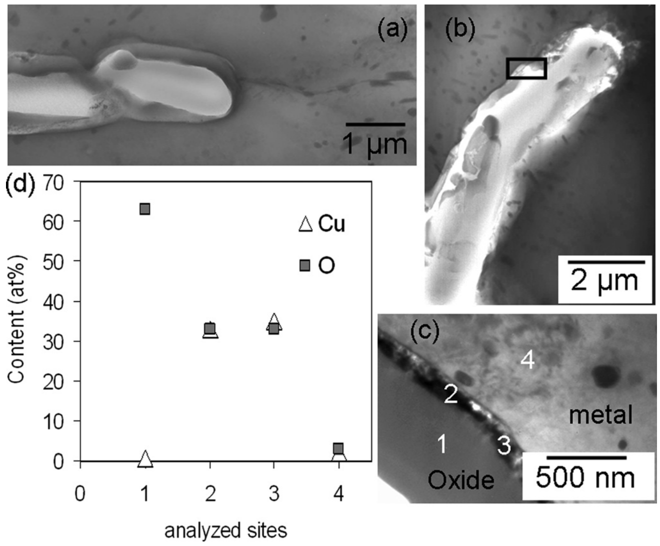

Figure 9. TEM observations of a corroded grain boundary after 72 h immersion in 1 M NaCl (a) global view (b) observation at the tip of the corrosion defect (c) close-up on the oxide formed on the corrosion defect walls (d) EDS analysis across the oxide.

compared to statistical analysis of the morphology of the corrosion defects and hydrogen content measurements) led us to assume that the mechanical stresses generated by frozen corrosion products were stronger that those generated by the dry or wet corrosion products and could favour another damaging process *i.e.* hydrogen penetration into the alloy. In order to validate these hypothesis, additional experiments were performed using a laser beam extensometer to check if the mechanical stresses generated by frozen electrolyte and/or corrosion products inside the corrosion defects were strong enough to be experimentally measured. Figure 10 shows the results obtained for samples exposed to a CF test. Results obtained for a non-corroded specimen are given for comparison. For this latter sample, the position of the target was quite stable as the non-corroded sample temperature increased. The experiment was performed four times and the results were reproducible; no mechanical stress was revealed as expected. For CF conditions, the deflection test was performed four times also with a different sample for each experiment. The curves obtained were not superimposed but they showed the same global shape with a sharp change at −17 °C followed by a slow decrease of the target position. For more clarity, only two examples of curves are given. The results showed that the sample was bent at the beginning of the deflection experiment which confirmed that, due to their volume expansion when they froze, the electrolyte and/or the corrosion products trapped inside the corrosion defects generated mechanical stresses strong enough to be revealed experimentally. This result supported the previous assumption concerning what could happen with the hydrogen produced due to H^+ reduction inside the corrosion defects of a CF sample and corroborated the hydrogen content measurements; for CF specimens, hydrogen transport was promoted during the air exposure period due to the mechanical stresses generated by frozen electrolyte and/or corrosion products and due to corresponding hydrogen/dislocations interactions. This phenomenon was added to classical hydrogen diffusion process which could occur only during the immersion period at room temperature since the hydrogen diffusion coefficient was very low at −20 °C. There was thus a volume degradation of 2024 alloy during CF corrosion tests due to the growth of a hydrogen-enriched zone at depth in the corrosion defects, which was larger than that of the corrosion defect itself. The results were fully consistent with the works performed by Pantelakis et al.[37] When the corroded specimens were submitted to a tensile test after the immersion test, the poor mechanical properties could be partially explained by an interaction between the hydrogen present in the enriched zone and the dislocations generated during the tensile tests. Furthermore, the mechanical stresses generated by the frozen electrolyte during the air exposure period could favor the opening of the corrosion defects and then accelerate their dissolution during the following immersion period. However, statistical data (Table II) showed that, for CF specimen, the propagation of corrosion defects was not promoted except for subgrain boundaries which were found to be corroded. Furthermore, it might be assumed also that the mechanical stresses generated weakened the oxide film which could initiate new corrosion defects explaining the high density of corrosion defects (Table II). Of course, the increase of corrosion defect density and the corrosion of subgrain boundaries contributed to the low residual mechanical properties measured during tensile tests for a sample exposed to CF tests. For continuously immersed samples and CR specimens, the lower hydrogen content measured suggested that hydrogen transport did not occur since the stresses related to wet or dry corrosion products were not strong enough; only hydrogen diffusion could be considered leading to lower hydrogen content. Therefore, it was concluded that, even if acidification at depth in the corrosion defect was a common feature for all corrosion conditions, the hydrogen effect was clearly visible only for CF samples due to the introduction of strong mechanical stresses during the air exposure period.

Measurements of the chloride concentration inside the corrosion defects.—Plate deflection technique was also used to determine the chloride concentration of the electrolyte trapped inside the intergranular corrosion defects (Fig. 10). For CF samples, the sharp change of the target position at −17 °C followed by a slow decrease evidenced the existence of a chloride gradient inside the corrosion defects as schematically explained in Fig. 11. During the corrosion test (step 2 in Fig. 4a), a chloride gradient was established as explained previously (step a in Fig. 11). When the sample was exposed to very cold temperatures during the deflection test (step 3 in Fig. 4a), the electrolyte with the lower chloride concentration far from the tip of the corrosion defect first froze (step b in Fig. 11). Then, the chloride-rich electrolyte at the tip of the corrosion defects froze leading, due the volume expansion generated, to the failure of the first frozen electrolyte (step c in Fig. 11). When the sample was warmed up (step d in Fig. 11), the chloride-rich electrolyte first melted leading to the closure of the crack generated in the first frozen electrolyte. This was evidenced on the curve by a sharp change of the target position. For CF samples, this sharp change occurred for a temperature of −17 °C which showed that a large part of the corrosion defects presented chloride concentration as high as 5 M at the tip of the corrosion defects. For other defects, the chloride gradient corresponded to chloride content at the tip of the defect lower than 5 M which explained the slow decrease of the target position. Therefore, for CF specimen, there were different populations of corrosion defects. For each population of corrosion defects, there was a chloride gradient inside the defects but one population differed from another by the chloride content reached at the tip of the corrosion defects, from 5 to 1 M. For CF specimen, there was a large population of corrosion defects with a 5 M chloride content at the tip. For CR samples, the curves obtained with the deflection test showed a similar shape which led us to give the same conclusions concerning the chloride concentration inside the corrosion defects. On the contrary, for the samples exposed to 24 and 72 h continuous immersion tests, only a continuous decrease of the target position was recorded when the sample temperature was increased. This showed that, for these last samples, there was also a chloride gradient inside the corrosion defects with different populations of corrosion defects; however, there was not a predominant population of corrosion defects. Therefore, the results showed that cyclic exposure to chloride solutions globally led to higher chloride concentration inside the corrosion defects compared to samples continuously immersed in such electrolytes. For CR samples, the chloride enrichment was related to the partial evaporation of the electrolyte trapped inside the corrosion

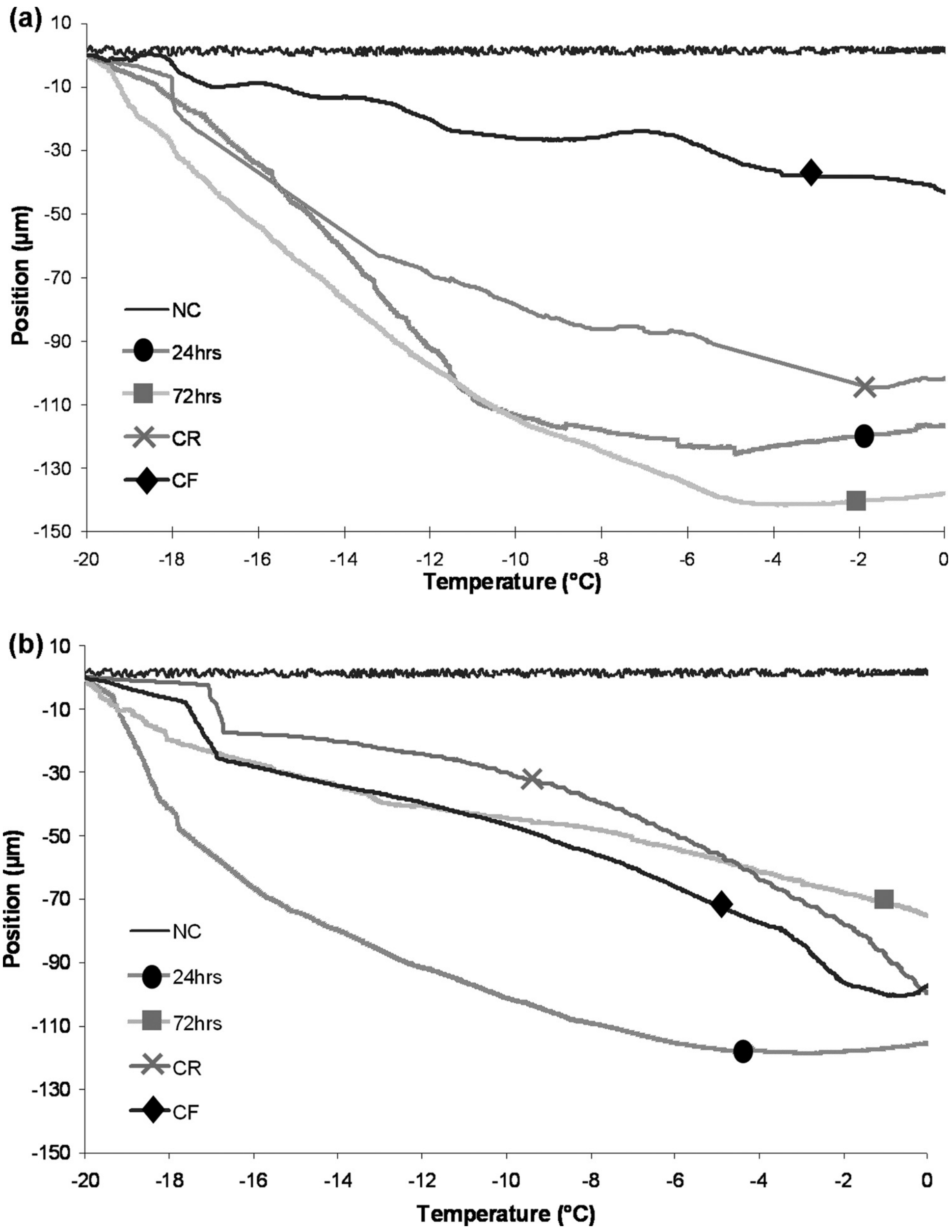

Figure 10. (a) Deflection tests performed on a non-corroded sample and on specimens exposed to a CF test, a CR test, a 24 and 72 h continuous immersion tests, first set of results (b) Deflection tests performed on a non-corroded sample and on specimens exposed to a CF test, a CR test, a 24 and 72 h continuous immersion tests, second set of results. For all the tests, the position of the target allowed the deflection of the specimens studied to be measured as the temperature rose.

defects during the air exposure periods at room temperature. For CF samples, the decrease of NaCl solubility in water at low temperature and subsequent salt precipitation inside the defects could be a valid hypothesis.

Electrochemical approach of the corrosion damage.—Concerning CR samples, previous results showing a high chloride concentration inside the corrosion defects were fully consistent with the statistical analysis of the corrosion damage. For CR corrosion tests, during the immersion period and for short defects, the cathodic reaction was mainly oxygen reduction on the sample surface while aluminum dissolved in the corrosion defects; rapid establishment of a chloride gradient inside the corrosion defects occurred. A high chloride concentration inside the corrosion defects promoted their propagation based on an autocatalytic process since the more the aluminum ions were produced, the more the chloride ions penetrated into the corrosion defects generating a more aggressive solution. However, the corrosion rate was limited by the oxygen reduction kinetics due to oxygen transport to the sample surface where the reaction took place. Corrosion products accumulated inside the corrosion defects so that there was rapidly little connection between the tip of the corrosion defects and the external electrolyte.[51] Therefore, during the air exposure periods and, for long corrosion defects during the immersion period, the main reaction was H^+ reduction inside the corrosion defects and the propagation rate of the corrosion defects mainly depended on local chemical conditions.[48,51] There was in this case no limitation by H^+ transport processes. Moreover, due to the formation of a Cu-rich film inside the corrosion defects, H^+ reduction was enhanced since its overpotential (and even that of oxygen reduction) was lower on Cu than on Al surface.[53] This led to an extensive propagation of the corrosion defects compared to continuous immersion tests. Figure 12 shows OCP measurements performed in 1 M NaCl solution at 22 °C for a sample exposed to a CR test; OCP values were measured at the beginning and at the end of each immersion period of the cyclic test. OCP versus continuous immersion time of an AA2024 sample was given for comparison.

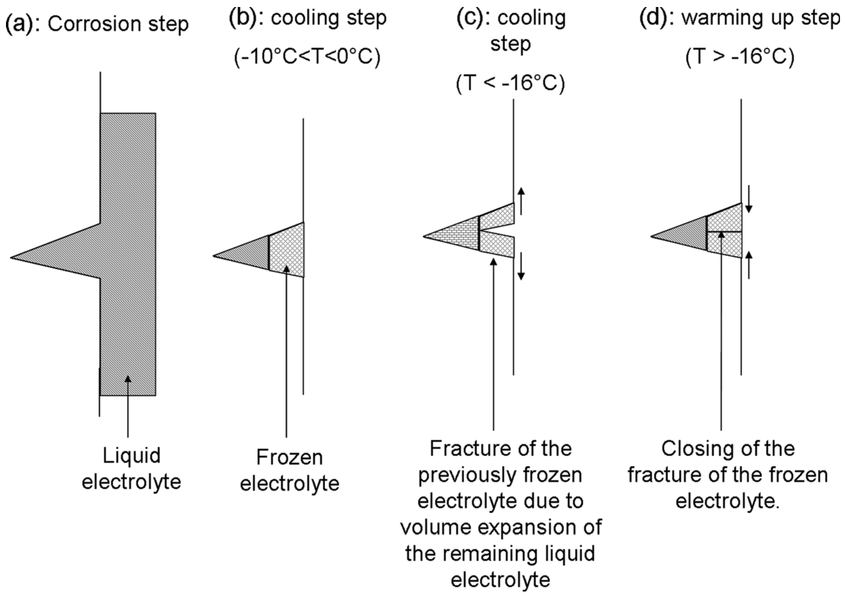

Figure 11. Schematical representation of the phase transformation occurring inside the corrosion defects during the deflection test.

For a continuous immersion in chloride solutions, the OCP markedly decreased during the first 24 h, which evidenced the propagation of the corrosion damage, and then stabilized at a value around −690 mV/SCE. For CR samples, the OCP values measured at the end of the corrosion test was lower, *i.e.*, around −725 mV/SCE, showing a more corroded sample. Furthermore, each air exposure period significantly influenced the electrochemical behavior of the sample with high OCP values measured at the end of the first and the second air exposure periods. This underlined the formation of an oxide film (and/or accumulation of corrosion products) on the sample surface during the air exposure periods[54] and therefore corroborated that the main reaction during the air exposure period and, for long defects during the immersion period, was H^+ reduction on the corrosion defect walls. Figure 13 shows the electrochemical impedance spectroscopy diagrams (Nyquist plots) plotted at the beginning of the corrosion tests and after each air exposure period for CR tests. Nyquist plots as a function of continuous immersion time in 1 M NaCl are given for comparison. Whatever the exposure conditions, the impedance diagrams were characterized by a capacitive loop in the high and medium frequency ranges. For continuous immersion in chloride solutions, the decrease in diameter of the capacitance loop when immersion time increased until 24 h evidenced the propagation of the corrosion damage. After 24, 48 and 72 h of immersion in 1 M NaCl, the Nyquist plots were nearly superimposed which corroborated the OCP results and showed a slowing down of the propagation of the corrosion defects for long immersion times. This was fully consistent with the statistical data of the corrosion morphology (Table II). For CR samples, the diameter of the capacitive loop was significantly lower at the beginning of the second cycle (after the first air exposure period) compared to that at the beginning of the corrosion test which evidenced the corrosion damage. After the second and the third air exposure periods, the diameter of the capacitive loop remained lower compared to that observed at the beginning of the corrosion test which was in good agreement with a corroded sample. However, this diameter was found to be higher than after the first air exposure periods which might be related to the formation of an oxide film on the sample surface and maybe to the accumulation of corrosion products due to the air exposure periods. It could be assumed that the partial drying of the corrosion products inside the corrosion defects during the air exposure period was perceived as the oxide layer healed and contributed, with the oxide film formed on the sample surface, to artificially and slightly hinder the corrosion damage on the Nyquist plots. Therefore, electrochemical impedance spectroscopy corroborated that the air exposure periods markedly influenced the electrochemical behavior of AA2024. The corrosion damage observed after a CR test was mainly explained taking into account electrochemical processes occurring as the tip of the defect which could be considered as an occluded zone characterized by a chloride-rich electrolyte and H^+ reduction as major cathodic reaction. Concerning CF samples, except for the OCP measured at the end of the first air exposure period, the OCP values monotonously decreased. The OCP values versus corrosion tests time were nearly superimposed with those obtained during a continuous immersion test with, at the end of the test, an OCP value lower for CF sample than for samples continuously immersed (Fig. 12). The results showed that, for CF samples, the air exposure periods were not efficient concerning the corrosion defects propagation which was related to the low temperature of the sample during the air exposure periods; no chemical processes could occur. Corrosion defects propagation occurred only during the immersion periods, the

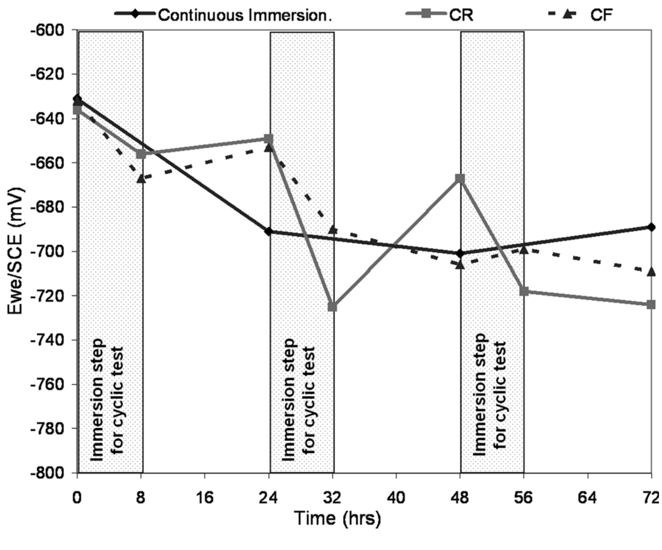

Figure 12. Open circuit potential (OCP) as a function of immersion time in 1 M NaCl solution at 22 °C for AA 2024 samples. For CR and CF samples, OCP was measured at the beginning and at the end of the immersion period for each of the three (immersion/air exposure period) cycles of the tests.

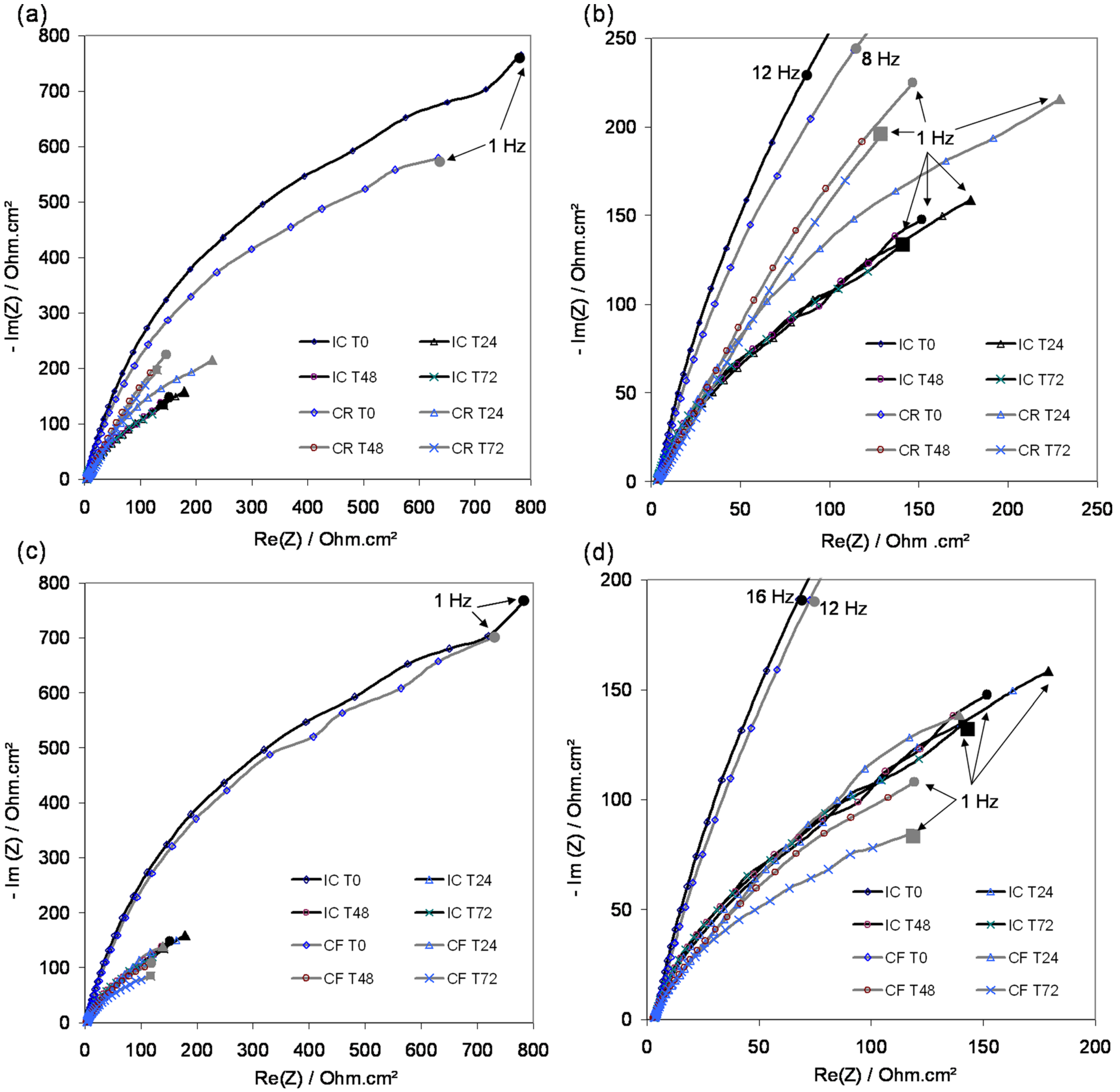

Figure 13. (Color online) Evolution of impedance diagrams (Nyquist plots) during corrosion tests for (a) CR samples (b) CR samples, zoom (c) CF samples (d) CF samples, zoom. The evolution of the impedance diagrams as a function of continuous immersion time in 1 M NaCl solution is given for comparison (IC).

main cathodic reaction being the oxygen reduction on the sample surface. This was similar with what happened for continuously immersed samples which corroborated the statistical data of the corrosion defects morphology with mean and maximal depth of the corrosion defects similar for CF samples and samples continuously immersed for 24 h (Table II). However, the lower values of the OCP at the end of the tests for CF samples could be related to the higher ratio of corroded grain boundaries and therefore to a more defective oxide film on the sample surface. This was in full agreement with the electrochemical impedance spectroscopy results (Fig. 13). After the first air exposure period, the capacitive loop for CF samples was quite superimposed with that corresponding to a sample continuously immersed for 24 h. Moreover, the diameter of the capacitive loop went on decreasing as the corrosion tests proceeded which could be related to an extension of the corrosion damage. The highly depressed shape of the capacitive loop suggested a defective oxide layer as that observed on a pitted surface which could be related to the high number of intergranular corrosion sites on the sample surface.[55] Electrochemical measurements were therefore in good agreement with the statistical analysis of the corrosion damage for CF samples (Table II) and the strong decrease of the mechanical properties observed (Fig. 5) had to be explained taking into account a hydrogen enriched zone at the tip of the corrosion defects promoted by the mechanical stresses generated by the frozen corrosion products during the air exposure periods.

Conclusions

Corrosion behavior of AA2024 was studied in chloride solution. The corrosion damage observed after continuous immersion tests was compared to that observed after cyclic tests. The main conclusions are:

1. Cyclic corrosion tests led to enhanced corrosion damage compared to continuous immersion tests with residual mechanical properties of corroded samples significantly lower for cyclic tests.
2. The corrosion defect morphology was significantly different depending on the exposure conditions and, in particular, on the temperature during the air exposure periods for cyclic tests. CR tests led to higher propagation of the corrosion defects compared to continuously immersed samples. For CF samples, the mean and maximal depth of corrosion defects were similar to those of a sample continuously immersed for 24 h but the ratio of corroded grain boundaries was markedly increased.
3. Concerning the electrochemical processes, common features were evidenced for all corrosion conditions with, in particular, the establishment of pH and chloride content gradients inside the corrosion defects. A deflection test, developed to measure the chloride concentration of the electrolyte trapped inside the corrosion defects, corroborated the results as well as hydrogen content measurements.
4. OCP and EIS measurements were consistent with the statistical analysis of the corrosion damage and underlined the strong influence of the air exposure periods on the electrochemical behavior of samples submitted to cyclic corrosion tests. For CR samples, as the corrosion defects propagated, they were rapidly isolated from the external environment due to accumulation of corrosion products and their partial drying during air exposure periods so that the propagation of corrosion defects only depended rapidly on local chemical conditions. For CF samples, the exposition to low temperatures led to a defective oxide film on the sample surface and stronger initiation for intergranular corrosion due to the mechanical stresses generated by frozen corrosion products on the corrosion defects walls. The deflection test allowed the mechanical stresses to be evidenced.
5. For CR tests, the dissolution processes and the morphology of the corrosion damage were in fully agreement with the residual mechanical properties. For CF tests, hydrogen embrittlement had to be taken into account to explain the global mechanical properties of the corroded samples.

Acknowledgments

This work was financially supported by the “Conseil Régional de la Région Midi-Pyrénées” and the “Ministère de l’Industrie” in the framework of the Diagnostat project. The authors thank S. Rolet (EADS IW) and N. Gouret (Airbus) for their help.

References

1. C. Blanc and G. Mankowski, *Corros. Sci.*, **40**, 411 (1998).
2. Z. Szklarska-Smialowska, *Corros. Sci.*, **41**, 1743 (1999).
3. N. D. Alexopoulos, *Mater. Sci. Eng., A*, **520**, 48 (2009).
4. W. Zhang and G. S. Frankel, *Electrochim. Acta*, **48**, 1193 (2003).
5. J. R. Galvele, *Corros. Sci.*, **47**, 3053 (2005).
6. V. Guillaumin and G. Mankowski, *Corros. Sci.*, **41**, 421 (1999).
7. J. R. Galvele and S. M. De Micheli, *Corros. Sci.*, **10**, 795 (1970).
8. C. Augustin, E. Andrieu, C. Blanc, G. Mankowski, and J. Delfosse, *J. Electrochem. Soc.*, **154**, C637 (2007).
9. W. Zhang and G. S. Frankel, *J. Electrochem. Soc.*, **149**, B510 (2002).
10. M. R. Bayoumi, *Eng. Fract. Mech.*, **54**, 879 (1996).
11. X. Liu, G. S. Frankel, B. Zoofan, and S. I. Rokhlin, *J. Electrochem. Soc.*, **153**, B42 (2006).
12. K. Urushino and K. Sugimoto, *Corros. Sci.*, **19**, 225 (1978).
13. M. A. Alodan and W. H. Smyrl, *J. Electrochem. Soc.*, **145**, 1571 (1998).
14. R. M. Rynders, C.-H. Paik, R. Ke, and R. C. Alkire, *J. Electrochem. Soc.*, **141**, 1439 (1994).
15. J. O. Park, C.-H. Paik, Y. H. Huang, and R. C. Alkire, *J. Electrochem. Soc.*, **146**, 517 (1999).
16. S. T. Pride, J. R. Scully, and J. L. Hudson, *J. Electrochem. Soc.*, **141**, 3028 (1994).
17. G. O. Ilevabare, O. Schneider, R. G. Kelly, and J. R. Scully, *J. Electrochem. Soc.*, **151**, B453 (2004).
18. K. Nisancioglu, *J. Electrochem Soc.*, **137**, 69 (1990).
19. R. G. Buchheit, R. P. Grant, P. F. Hlava, B. McKenzie, and G. L. Zender, *J. Electrochem. Soc.*, **144**, 2621 (1997).
20. N. Birbilis, M. K. Cavanaugh, and R. G. Buchheit, *Corros. Sci.*, **48**, 4202 (2006).
21. N. Dimitrov, J. A. Mann, and K. Sieradzki, *J. Electrochem. Soc.*, **146**, 98 (1999).
22. L. Lacroix, L. Ressier, C. Blanc, and G. Mankowski, *J. Electrochem. Soc.*, **155**, C131 (2008).
23. L. Lacroix, L. Ressier, C. Blanc, and G. Mankowski, *J. Electrochem. Soc.*, **155**, C8 (2008).
24. K. Sasaki, P. W. Levy, and H. S. Isaacs, *Electrochem. Solid-State Lett.*, **5**, B25 (2002).
25. M. A. Jakab, D. A. Little, and J. R. Scully, *J. Electrochem. Soc.*, **152**, B311 (2005).
26. G. S. Chen, M. Gao, and R. P. Wei, *Corrosion (Houston)*, **52**, 8 (1996).
27. A. Hughes, T. H. Muster, A. Boag, A. M. Glenn, C. Luo, X. Zhou, G. E. Thompson, and D. McCulloch, *Corros. Sci.*, **52**, 665 (2010).
28. A. Boag, A. E. Hughes, A. M. Glenn, T. H. Muster, and D. McCulloch, *Corros. Sci.*, **53**, 17 (2011).
29. A. E. Hughes, A. Boag, A. M. Glenn, D. McCulloch, T. H. Muster, C. Ryan, C. Luo, X. Zhou, and G. E. Thompson, *Corros. Sci.*, **53**, 27 (2011).
30. A. M. Glenn, T. H. Muster, C. Luo, X. Zhou, G. E. Thompson, A. Boag, and A. E. Hughes, *Corros. Sci.*, **53**, 40 (2011).
31. T. Hashimoto, X. Zhou, C. Luo, K. Kawano, G. E. Thompson, A. E. Hughes, P. Skeldon, P. J. Withers, T. J. Marrow, and A. H. Sherry, *Scr. Mater.*, **63**, 835 (2010).
32. S. P. Knight, M. Salagaras, A. M. Wythe, F. De Carlo, A. J. Davenport, and A. R. Trueman, *Corros. Sci.*, **52**, 3855 (2010).
33. M. J. Robinson and N. C. Jackson, *Corros. Sci.*, **41**, 1013 (1999).
34. X. Liu, G. S. Frankel, B. Zoofan, and S. I. Rokhlin, *Corros. Sci.*, **46**, 405 (2004).
35. X. Liu and G. S. Frankel, *Corros. Sci.*, **48**, 3309 (2006).
36. C. Augustin, E. Andrieu, C. Baret-Blanc, J. Delfosse, and G. Odemer, *J. Electrochem. Soc.*, **157**, C428 (2010).
37. S. G. Pantelakis, P. G. Daglaras, and C. A. Apostolopoulos, *Theor. Appl. Fract. Mech.*, **33**, 117 (2000).
38. P. C. King, I. S. Cole, P. A. Corrigan, A. E. Hughes, and T. H. Muster, *Corros. Sci.*, **53**, 1086 (2011).
39. M. B. Vukmirovic, N. Dimitrov, and K. Sieradski, *J. Electrochem. Soc.*, **149**, B428 (2002).
40. C. Blanc, B. Lavelle, and G. Mankowski, *Corros. Sci.*, **39**, 495 (1997).
41. C. Blanc, A. Freulon, M. C. Lafont, Y. Kihn, and G. Mankowski, *Corros. Sci.*, **48**, 3838 (2006).
42. F. Eckermann, Th. Suter, P. J. Uggowitzer, A. Afseth, A. J. Davenport, B. J. Connolly, M. H. Larsen, F. De Carlo, and P. Schmutz, *Corros. Sci.*, **50**, 3455 (2008).
43. S. P. Knight, N. Birbilis, B. C. Muddle, A. R. Trueman, and S. P. Lynch, *Corros. Sci.*, **52**, 4073 (2010).
44. J. Idrac, C. Blanc, Y. Kihn, M. C. Lafont, G. Mankowski, P. Skeldon, and G. Thompson, *J. Electrochem. Soc.*, **154**, C286 (2007).
45. J. Idrac, G. Mankowski, G. Thompson, P. Skeldon, Y. Kihn, and C. Blanc, *Electrochim. Acta*, **52**, 7626 (2007).
46. K. Shimizu, G. M. Brown, H. Habazaki, K. Kobayashi, G. E. Thompson, P. Skeldon, and G. C. Wood, *Corros. Sci.*, **41**, 1783 (1999).
47. K. Shimizu, G. M. Brown, H. Habazaki, K. Kobayashi, G. E. Thompson, P. Skeldon, and G. C. Wood, *Corros. Sci.*, **42**, 831 (2000).
48. S. P. Knight, M. Salagaras, and A. R. Trueman, *Corros. Sci.*, **53**, 727 (2011).
49. D. McNaughtan, H. W. Van Rooijen, E. P. M. Van Westing, and J. H. W. De Wit, *Corros. Sci.*, **45**, 2377 (2003).
50. D. McNaughtan, M. Worsfold, and M. J. Robinson, *Corros. Sci.*, **45**, 2377 (2003).
51. T.-S. Huang and G. S. Frankel, *Corros. Sci.*, **49**, 858 (2007).
52. M. J. Robinson, *Corros. Sci.*, **23**, 887 (1983).
53. R. G. Buchheit, R. K. Boger, M. C. Carroll, R. M. Leard, C. Paglia, and J. L. Searles, *JOM*, **53**, 29 (2001).
54. R. E. Lobnig, D. J. Siconolfi, J. Maisano, G. Grundmeier, H. Streckel, R. P. Frankenthal, M. Stratmann, and J. D. Sinclair, *J. Electrochem. Soc.*, **143**, 1175 (1996).
55. M. Keddam, C. Kuntz, H. Takenouti, D. Schuster, and D. Zuili, *Electrochim. Acta*, **42**, 87 (1997).